Mitigating Laser Imprint in Direct-Drive Inertial Confinement Fusion Implosions with High-Z Dopants

S. X. Hu (□□□), G. Fiksel, V. N. Goncharov, S. Skupsky, D. D. Meyerhofer, and V. A. Smalyuk

Phys. Rev. Lett. **108**, 195003 — Published 8 May 2012

DOI: 10.1103/PhysRevLett.108.195003

Mitigating laser imprint in direct-drive ICF implosions with high-*Z* dopants

S. X. Hu(胡素兴)*, G. Fiksel, V. N. Goncharov, S. Skupsky, and D. D. Meyerhofer

Laboratory for Laser Energetics, University of Rochester,

250 E. River Road, Rochester, New York 14623, USA

V. A. Smalyuk

Lawrence Livermore National Laboratory, Livermore, California 94551, USA

Abstract

Nonuniformities seeded by both long- and short-wavelength laser perturbations can grow via Rayleigh–Taylor (RT) instability in direct-drive inertial confinement fusion (ICF), leading to performance reduction in low-adiabat implosions. To mitigate the effect of laser-imprinting on target performance, spherical RT experiments have been performed on OMEGA using Si-/Ge-doped plastic targets in a cone-in-shell configuration. Compared to a pure plastic target, radiation preheating from these high-*Z* dopants (Si/Ge) increases the ablation velocity and the standoff distance between the ablation front and laser-deposition region, thereby reducing both the imprinting efficiency and the RT growth rate. Experiments showed a factor of 2 ~ 3 reduction in the laser-imprinting efficiency and a reduced RT growth rate, leading to significant (3 ~ 5 times) reduction in the σ_{rms} of shell ρR modulation for Si-/Ge-doped targets. These features are reproduced by radiation–hydrodynamics simulations using the two-dimensional hydrocode *DRACO*.

PACS numbers: 52.57.Fg, 52.35.Py
*Corresponding author and E-mail: shu@lle.rochester.edu

Rayleigh–Taylor (RT) instability,[1] one of the hydrodynamic instabilities that may compromise inertial confinement fusion (ICF) target performance, is inevitable in ICF implosions since the imploding shell (heavy fluid) is accelerated by the blowoff plasmas (light fluid). Perturbations seeded by target roughness and laser nonuniformities can grow via RT instability, thereby affecting the target compression and degrading the neutron-yield.[2,3] Because of its importance to ICF, the RT instability in ICF-relevant plasmas has been studied both in experiments[4–8] and in theory/simulations.[9–13] For ICF ignition implosions,[14,15] the laser-beam intensity nonuniformities that imprint on the target can be amplified during the shell's acceleration phase. Controlling the RT instability, by lowering the amplitudes of laser imprinting and reducing its growth rate, is crucial for direct-drive–ignition target designs. Laser imprinting can be controlled by (a) making laser beams as smooth as possible by using distributed phase plates (DPP's),[16] applying temporal speckle-averaging techniques,[17] and polarization smoothing;[18] (b) designing pulse shapes that can reduce the RT growth rate, for instance, by "adiabat shaping" with picket pulses;[19–21] and (c) optimizing ICF target ablators, for example, by using foam targets[22,23] and laminated ablators.[24,25]

Studies have also been made of using high-Z, thin-layer ablation coating on plastic (CH) capsules to reduce laser imprinting.[26–28] The idea of coating high-Z (Au/Pd), thin (<1000 Å) layers to reduce laser imprinting came about because the high-Z ablation layers quickly expand and convert the initial nonuniform laser flux into uniform x-ray radiation to ablate the target. Implosions with such high-Z–layered targets have shown a factor-of-2 increase in yield as evidence of improved target stability.[28] Instead of using high-Z thin layers, high-Z doping into the CH ablator layer not only can serve the same purpose of suppressing laser imprinting, but also can reduce the RT growth rate due to the enhanced radiation preheat at the ablation

surface. When Si-/Ge-doped plastic targets have been imploded on OMEGA, more than a factor-of-2 increase in neutron yield has been observed.[29] This has been attributed to possible improvements in target stability. So far, however, no direct measurements have shown the expected perturbation reduction in such high-Z–doping targets. In this Letter, we present for the first time such direct measurements of spherical RT growth in implosions of high-Z–doped plastic capsules. Compared to pure plastic targets, high-Z–doped targets showed a factor of 2 ~ 3 reduction in the laser-imprinting level and ~1.5 times decrease in the RT growth rate. At the end of shell acceleration, significant reduction (by 3 ~5 times) in shell ρR modulation has been observed for high-Z–doped targets. These features have been reproduced by two-dimensional (2-D) radiation hydrodynamics simulations.

The rationale of using high-Z doping to mitigate laser-imprinting effects in direct-drive ICF target implosions is two-fold: (1) the quick absorption and expansion of a high-Z–doped ablator may decrease the imprinting efficiency caused by the fast formation of a standoff plasma; and (2) the radiation preheating at the ablation front could increase the ablation velocity and, in turn, enhance the ablative stabilization of RT growth. To illustrate these points, we have performed radiation–hydrodynamics simulations of pure CH targets in comparison with 7.4% (atomic fraction) Si-doped CH targets (CHSi[7.4%]) using the one-dimensional (1-D) hydrocode *LILAC*.[30] These capsules have a diameter of ~860 μm and a shell thickness of ~22.5 μm. The low-adiabat triple-picket laser pulse, shown by Fig. 1(a), is used to implode such targets. Figures 1(c) and 1(d) show the density profiles (red solid lines) and the spatial distributions of laser depositions (blue lines) at t = 0.5 ns predicted by *LILAC* simulations for the pure-CH target and the CHSi[7.4%] case, respectively. One sees that the standoff distance between the laser-absorption region to the ablation front (conventionally defined at the position

where the density is about 1/*e* of peak density) increases from ~10 μm of the pure-CH case to ~15 μm for the Si-doped CH target. The right vertical lines in Figs. 1(c) and 1(d) mark the inner position of laser deposition, which are chosen to be the inward 1/e of the peak deposition. The longer standoff plasmas allow more thermal smoothing of short-wavelength laser perturbations, reducing the laser-imprinting level on the Si-doped target. Moreover, since the entire target has been Si-doped, the enhanced coronal radiation continuously preheats the CHSi ablation surface. This increases the time-averaged ablation velocity from $V_a \approx 4.5$ μm/ns of the CH target to $V_a \approx$ 10.0 μm/ns for the CHSi[7.4%] target. According to the fitting formula of linear RT growth,[31] $\Gamma_k = 0.94\sqrt{kg/(1+kL_n)} - 1.5\, kV_a$ for modulation wave number k with the acceleration g and density scale length L_n at the ablation front, the increased ablation velocity in the Si-doped CH target reduces the RT growth rate and moves the "cutoff wavelength" to longer ones, as shown in Fig. 1(b). The time-averaged accelerations are g = 110 μm/ns^2 and g= 120 μm/ns^2 respectively for the two cases of CH and CHSi[7.4%]. The radiation preheating increases the adiabat at the ablation surface as well as its density scale-length (L_n=3.0 μm and L_n=3.5 μm respectively for the pure CH target and the CHSi[7.4%] target), which also partially contributes to the RT growth reduction according to the above formula.

To benchmark the laser-imprinting reduction effects predicted by the above hydro-simulations, spherical RT experiments with high-*Z*–doped plastic capsules in the cone-in-shell configuration[32,33] have been conducted at the Omega Laser Facility. A schematic diagram of the experimental setup is shown in Fig. 2. A plastic spherical shell with an 860-μm diameter and a 400-μm opening is attached to an open gold cone with a 3.5-mm maximum diameter and a 53° cone angle. The OMEGA beams originally illuminating the cone part are turned off. For

these experiments pure plastic (CH) shells as well as doped CH shells with atomic fractions of 4.3% Si, 7.4% Si, and 3.9% Ge were used. The shell thickness varied slightly from 22.1 μm to 22.8 μm, and the high-Z doping was made through the entire capsule. The targets were imploded by 48 OMEGA beams with the low-adiabat laser pulse shown in Fig. 1(a). Laser imprinting is imposed by the broadband intensity modulations of the distributed phase plates (DPP's). It creates a broadband spectrum of perturbations in laser intensity on the target surface, while smoothing by spectral dispersion (SSD) is turned off. The shell was imaged by x rays using a tantalum (Ta) foil backlighter irradiated by an additional six OMEGA beams. The x rays, with a peak energy around $h\nu \sim 2.8$ keV, propagated through the shell and the opening cone and were recorded by an x-ray framing camera (XRFC), with a spatial resolution of ~10 μm and temporal resolution of ~80 ps. A maximum of 16 images were recorded for each shot at different times to trace the perturbation growth in the shell ρR.

To investigate the laser imprinting and its RT growth in such spherical experiments, two-dimensional (2-D) radiation–hydrodynamics simulations have been performed for each shot using our 2-D hydrocode *DRACO*.[34] This 2-D hydrocode has been extensively benchmarked with a variety of experiments in both planar and spherical geometries.[32,33,35–39] The flux-limited ($f = 0.06$) thermal transport model has been used in these 2-D simulations. Cross-beam energy transfer (CBET)[40] was effectively taken into account using a slightly reduced drive. For the radiation transport, the Astrophysical Opacity Tables[41] (AOT) were applied for the CH target, while the non-local-thermodynamic-equilibrium (NLTE) opacity tables (based on the average-ion model[42]) was used for the Si-/Ge-doped targets. For the pure CH target, the NLTE average-ion table is essentially equivalent to the AOT table, because only low-Z species are involved in the CH plasma. The laser

perturbations up to a maximum DPP-mode ℓ = 400 (corresponding to the shortest wavelength of $\lambda_{\min}$ = 6.75 μm) have been included. As an example, the snapshots of density contours at t = 1.5 ns are plotted in Figs. 3(a) and 3(b) for the imploding CH shell and CHSi[7.4%] shell, respectively. The insets in Figs. 3(a) and 3(b) give zoomed views of the shell density perturbations for the two cases. It can be seen that the 7.4%-Si–doped CH shell in Fig. 3(b) is much smoother than the pure-CH target. The calculated $\sigma_{\text{rms}}[\rho R]$ is ~0.035 mg/cm^2 for the CHSi[7.4%] target, in contrast to $\sigma_{\text{rms}}[\rho R] \simeq$ 0.086 mg/cm^2 in the pure-CH shell. A factor of ~2.5 reduction in the laser-imprinting level was predicted for the CHSi[7.4%] target.

The subsequent RT growth will further amplify the imprinted perturbations during the shell acceleration. When the shell converges to a radius of $R \sim 200$ μm, the density profiles for the above studied cases were plotted in Figs. 4(a) and 4(b). The corresponding experimental raw images are also shown by Figs. 4(c) and 4(d), respectively for the pure-CH target and the CHSi[7.4%] target. For the pure-CH target, Fig. 4(a) indicates that the shell is "broken" with significant density modulations, while the integrity of the CHSi[7.4%] target is much better than the pure-CH case. The inner surface of the CHSi[7.4%] shell is much smoother, which can significantly lower the perturbation seeding level for the deceleration-phase RT growth. The corresponding experimental image of x-ray intensity distribution in Fig. 4(d) shows less variation in the Si-doping target, in contrast to the highly nonuniform image of the CH target.

The measured optical-depth modulations Δ_{OD} can be related to the shell's areal-density perturbations $\Delta_{\rho R}$ through the approximated relationship of $\Delta_{\text{OD}} = \bar{\mu}\Delta_{\rho R}$, utilizing the fact that $\bar{\mu}$ is a slowly varied quantity for the shell plasma conditions being probed. By using undriven targets with an additional 200-μm open hole in the capsule (within the x-ray–viewing window),

we have determined the mass-absorption coefficients $\bar{\mu}$ for each of these capsules using the same Ta backlighter: $\bar{\mu}$ = 109.7±25.8 cm^2/g, 317.4±46.9 cm^2/g, 400.2±52.2 cm^2/g, and 517.1±46.0 cm^2/g for targets of pure CH, CHSi[4.3%], CHSi[7.4%], and CHGe[3.9%], respectively. These numbers are comparable to theoretical calculations using the Astrophysical Opacity Tables[41] for the CH target and the averaged-ion (NLTE) opacity tables for the Si-/Ge-doped targets. To be specific, the calculated mass-absorption coefficients $\bar{\mu}$ for these materials are 135 cm^2/g, 308 cm^2/g, 415 cm^2/g, and 525 cm^2/g, respectively. Using these mass-absorption coefficients, the σ_{rms} of shell ρR modulation can be obtained directly from experimentally recorded Δ_{OD}. The experimental results are plotted in Fig. 5 with blue circles (CH), green squares (CHSi[4.3%]), red diamonds (CHSi[7.4%]), and open black triangles (CHGe[3.9%]), respectively. They are compared with the *DRACO* simulations represented by the corresponding colored lines. The experimentally measured backlighter spectrum and the spatial/temporal resolutions of the x-ray framing camera have been used for post-processing the 2-D simulations to obtain the areal-density modulations, which are directly compared with experimental measurements. Overall, the 2-D simulations reproduce the trends observed in experiments, which are the reduced imprinting level and lower RT growth rate of the high-*Z*–doped targets, when compared to the pure-CH–target implosion. Specifically, the high-*Z* doping has reduced the imprinting level by a factor of ~2 for CHSi[4.3%] and by a factor of 2.5 ~ 3 for CHSi[7.4%] and CHGe[3.9%]; the measured σ_{rms} growth rate of ρR perturbations in Si-/Ge-doped targets are decreased from ~1.5±0.1 ns^{-1} of the pure CH target to ~1.24±0.08 ns^{-1} (CHSi[4.3%]), ~1.06±0.09 ns^{-1} (CHSi[7.4%]), and ~0.89±0.1 ns^{-1} (CHGe[3.9%]), respectively. Performing the wavelength-averaging for the growth rate up to the open-cone

dimension ($\lambda \approx 400$ μm), the analytical formula[31] predicted a wavelength-averaged RT growth rate of $\tilde{\Gamma} \sim 1.51$ ns^{-1} (CH), $\tilde{\Gamma} \sim 1.26$ ns^{-1} (CHSi[4.3%]), $\tilde{\Gamma} \sim 1.18$ ns^{-1} (CHSi[7.4%]), and $\tilde{\Gamma} \sim 1.08$ ns^{-1} (CHGe[3.9%]), in good agreement with measurements. The σ_{rms} of shell ρR has been reduced by 3 ~ 5 times in high-*Z*–doped targets near the end of acceleration. It is noted that the early-time discrepancy between the experiments and simulations are originated from the fact that the signals are just above the background noise. This is the origin of the big error bars for the experimental points at the early stage of RT growth.

In summary, we have directly measured the broadband laser imprinting and its RT growth in direct-drive spherical implosions using high-*Z*–doped targets. In agreement with two-dimensional *DRACO* simulations, experimental measurements indicated that a few percent of Si-/Ge-doping can reduce the laser-imprinting level by ~2 to 3 times and decrease the RT growth rate by a factor of ~1.5, when compared to the pure-CH–target implosion. High-*Z* doping can reduce the σ_{rms} of target perturbations by ~3 to 5 times at the end of acceleration, depending on the dopants and their concentrations. These observations would facilitate high-gain ignition target designs with high-*Z*–doped ablators. For cryogenic-DT–ignition designs, radiation preheat can be minimized by controlling the doping-layer thickness, in addition to using the transparency of DT fuels to 2~3-keV coronal radiations. Namely, to prevent the radiation preheating DT fuels, we have controlled the high-Z doping only to the outmost several micrometers of the CH ablator. Thus, the left un-doped CH layer could reduce the radiation penetration into the fuel. Simulations have shown negligible radiation preheat effects for the direct-drive NIF ignition design using a half-Si-doped and half-undoped CH ablator.

Acknowledgment

This work was supported by the U.S. Department of Energy Office of Inertial Confinement Fusion under Cooperative Agreement No. DE-FC52-08NA28302, the University of Rochester, and the New York State Energy Research and Development Authority. The support of DOE does not constitute an endorsement by DOE of the views expressed in this article.

REFERENCES

[1] Lord Rayleigh, Proc. London Math Soc. **XIV**, 170 (1883); G. Taylor, Proc. R. Soc. London Ser. A **201**, 192 (1950).

[2] S. E. Bodner, Phys. Rev. Lett. **33**, 761 (1974).

[3] S. Atzeni and J. Meyer-ter-Vehn, *The Physics of Inertial Fusion: Beam Plasma Interaction, Hydrodynamics, Hot Dense Matter*, International Series of Monographs on Physics (Clarendon Press, Oxford, 2004).

[4] B. A. Remington *et al.*, Phys. Rev. Lett. **73**, 545 (1994).

[5] S. G. Glendinning *et al.*, Phys. Rev. Lett. **78**, 3318 (1997).

[6] H. Azechi *et al.*, Phys. Plasmas **4**, 4079 (1997); H. Azechi *et al.*, Phys. Rev. Lett. **98**, 045002 (2007).

[7] C. Cherfils *et al.*, Phys. Rev. Lett. **83**, 5507 (1999).

[8] V. A. Smalyuk *et al*., Phys. Rev. Lett. **81**, 5342 (1998); *ibid* **95**, 215001 (2005).

[9] H. Takabe *et al.*, Phys. Fluids **28**, 3676 (1985).

[10] S. W. Haan, Phys. Rev. A **39**, 5812 (1989).

[11] J. Sanz, Phys. Rev. Lett. **73**, 2700 (1994).

[12] V. N. Goncharov *et al.*, Phys. Plasmas **3**, 1402 (1996).

[13] M. M. Marinak *et al.*, Phys. Rev. Lett. **80**, 4426 (1998).

[14] R. L. McCrory *et al.*, Phys. Plasmas **15**, 055503 (2008); D. D. Meyerhofer *et al.*, Nucl. Fusion **51**, 053010 (2011).

[15] C. Cherfils-Clérouin *et al.*, J. Phys.: Conf. Ser. **244**, 022009 (2010).

[16] Y. Kato *et al.,* Phys. Rev. Lett. **53**, 1057 (1984); Y. Lin, T. J. Kessler, and G. N. Lawrence, Opt. Lett. **20**, 764 (1995).

[17] R. H. Lehmberg, A. J. Schmitt, S. E. Bodner, J. Appl. Phys. **62**, 2680 (1987); S. Skupsky *et al.*, J. Appl. Phys. **66**, 3456 (1989).

[18] T. R. Boehly *et al.*, J. Appl. Phys. **85**, 3444 (1999).

[19] V. N. Goncharov *et al.*, Phys. Plasmas **10**, 1906 (2003).

[20] N. Metzler *et al.*, Phys. Plasmas **10**, 1897 (2003).

[21] V. N. Goncharov *et al.*, Phys. Rev. Lett. **104**, 165001 (2010).

[22] R. J. Mason *et al.*, Phys. Plasmas **5**, 211 (1998).

[23] R. G. Watt *et al.*, Phys. Rev. Lett. **81**, 4644 (1998); S. Depierreux *et al*., Phys. Rev. Lett. **102**, 195005 (2009).

[24] L. Masse, Phys. Rev. Lett. **98**, 245001 (2007).

[25] L. Masse *et al.*, Phys. Rev. E **83**, 055401(R) (2011).

[26] S. P. Obenschain *et al.*, Phys. Plasmas **9**, 2234 (2002).

[27] M. Karasik *et al.*, Bull. Am. Phys. Soc. **49**, 276 (2004).

[28] A. N. Mostovych *et al.*, Phys. Rev. Lett. **100**, 075002 (2008).

[29] V. N. Goncharov *et al.*, Phys. Plasmas **15**, 056310 (2008).

[30] J. Delettrez *et al.*, Phys. Rev. A **36**, 3926 (1987).

[31] R. Betti *et al.*, Phys. Plasmas **5**, 1446 (1998).

[32] V. A. Smalyuk *et al.*, Phys. Rev. Lett. **103**, 105001 (2009).

[33] V. A. Smalyuk *et al.*, Phys. Plasmas **16**, 112701 (2009).

[34] D. Keller *et al.*, Bull. Am. Phys. Soc. **44**, 37 (1999); P. B. Radha *et al.*, Phys. Plasmas **12**, 056307 (2005).

[35] S. X. Hu *et al*., Phys. Rev. Lett. **100**, 185003 (2008); *ibid* **101**, 055002 (2008).

[36] S. X. Hu *et al*., Phys. Plasmas **16**, 112706 (2009); *ibid* **17**, 102706 (2010).

[37] I. V. Igumenshchev *et al.*, Phys. Plasmas **16**, 082701 (2009).

[38] V. A. Smalyuk *et al.*, Phys. Rev. Lett. **101**, 025002 (2008).

[39] V. A. Smalyuk *et al.*, Phys. Plasmas **15**, 082703 (2008).

[40] I. V. Igumenshchev *et al.*, Phys. Plasmas **17**, 122708 (2010).

[41] W. F. Huebner *et al.*, Los Alamos National Laboratory, Los Alamos, NM, Report LA-6760-M (1977).

[42] H. Takabe and T. Nishikawa, J. Quant. Spectrosc. Radiat. Transf. **51**, 379 (1994).

FIGURE CAPTIONS

FIG. 1: (Color online) (a) The triple-picket plus main-square pulse shape used for our spherical RT experiments; and (b) the growth rates as a function of perturbation wavelength are compared for the pure CH target (red solid line) and the CHSi[7.4%] target (blue line). The spatial profiles of both density (red/solid line) and laser-deposition (blue line) are plotted as a function of target radius at t = 0.5 ns, respectively for (c) the pure CH target and (d) the Si-doped CH target (CHSi[7.4%]).

FIG. 2: (Color online) The schematic diagram of cone-in-shell configuration used in our spherical RT experiments with Si-/Ge-doped plastic targets.

FIG. 3: (Color online) The density contour plots at the beginning of acceleration, t = 1.5 ns, from *DRACO* simulations of (a) the pure-CH target and (b) the CHSi[7.4%] target. The insets show the zoomed view for the selected portion of the shell.

FIG. 4: (Color online) The density contour plots predicted by *DRACO* simulations near the end of acceleration, for the similar distance traveled by the shells: (a) the pure-CH target (t=2.40 ns) and (b) the CHSi[7.4%] target (t=2.54 ns). The experimental raw images depicted in (c) and (d), respectively for these two cases, represent the x-ray intensity variation recorded on CCD.

FIG. 5: (Color online) The comparison of measured σ_{rms} of ρR modulations with *DRACO* simulations as a function of time, for targets of pure-CH (blue/circles), CHSi[4.3%] (green squares), CHSi[7.4%] (red diamonds), and CHGe[3.9%] (black open deltas). The same colored solid lines are from *DRACO* simulations for the corresponding shots.

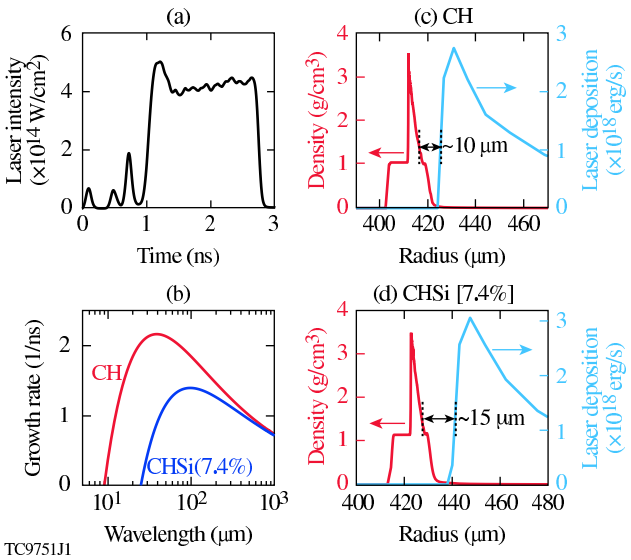

Figure 1 LL13576 20MAR2012

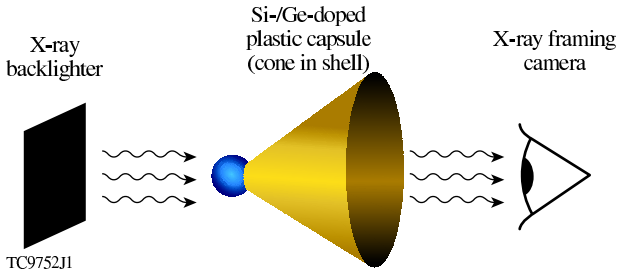

Figure 2 LL13576 20MAR2012

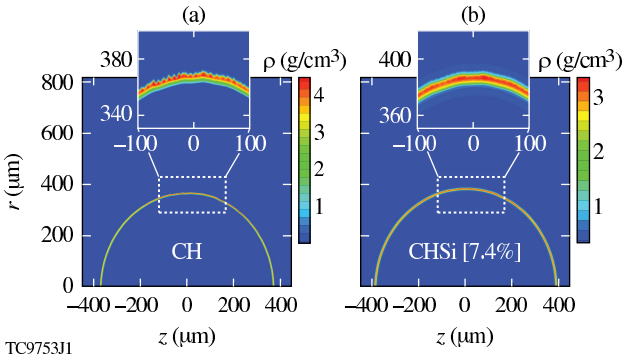

Figure 3 LL13576 20MAR2012

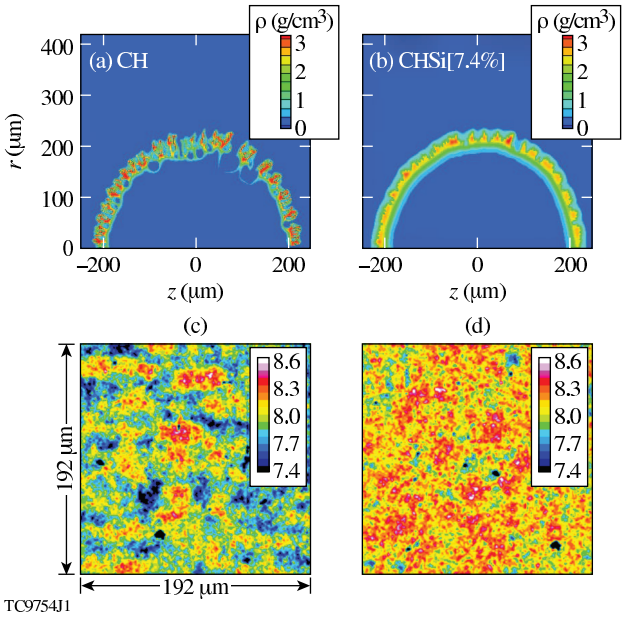

Figure 4 LL13576 20MAR2012

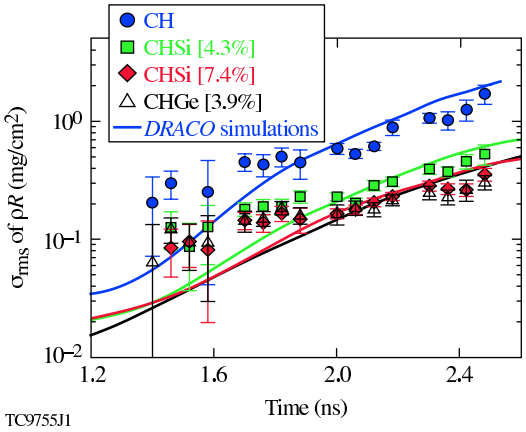

Figure 5 LL13576 20MAR2012